

## Light soaking in metal halide perovskites studied via steady-state microwave conductivity

C Lowell Watts <sup>1</sup>, Lee Aspitarte <sup>2</sup>, Yen-Hung Lin <sup>3</sup>, Wen Li<sup>3,4</sup>, Radwan Elzein <sup>5</sup>, Rafik Addou <sup>5</sup>, Min Ji Hong <sup>1</sup>, Gregory S. Herman<sup>5</sup>, Henry J. Snaith <sup>3</sup> & John G. Labram <sup>1</sup>✉

The light-soaking effect is the observation that under constant illumination the measured power conversion efficiency of certain solar cells changes as a function of time. The theory of the light-soaking in metal halide perovskites is at present incomplete. In this report, we employ steady-state microwave conductivity, a contactless probe of electronic properties of semiconductors, to study the light-soaking effect in metal halide perovskites. By illuminating isolated thin films of two mixed-cation perovskites with AM1.5 solar illumination, we observe a continual increase in photoconductance over a period of many (>12) hours. We can fit the experimentally observed changes in photoconductance to a stretched exponential function, in an analogous manner to bias-stressed thin-film transistors. The information provided in this report should help the community better understand one of the most perplexing open problems in the field of perovskite solar cells and, ultimately, lead to more robust and predictable devices.

<sup>1</sup>School of Electrical Engineering and Computer Science, Oregon State University, Corvallis, OR 97331, USA. <sup>2</sup>Department of Physics, Oregon State University, Corvallis, OR 97331, USA. <sup>3</sup>Clarendon Laboratory, Department of Physics, University of Oxford, Parks Road, Oxford OX1 3PU, UK. <sup>4</sup>Institute of Flexible Electronics (IFE), Northwestern Polytechnical University, Xi'an 710072, China. <sup>5</sup>School of Chemical, Biological and Environmental Engineering, Oregon State University, Oregon, OR 97331, USA. ✉email: [john.labram@oregonstate.edu](mailto:john.labram@oregonstate.edu)

Although metal halide perovskites (MHPs) offer the community many exciting opportunities<sup>1</sup>, consistent understanding and consensus still lags behind more long-studied systems such as organic semiconductors<sup>2</sup> or silicon<sup>3</sup>. Developing a robust understanding of this class of materials is paramount to their future success as a commercial technology. The light soaking effect in MHPs is an example of a phenomenon, which is still lacking a consistent description from the community<sup>4–8</sup>. Light soaking is the observation that the measured power conversion efficiency (PCE) of certain solar cells changes as a function of time, under constant illumination<sup>9</sup>. This is a phenomenon observed in wide-range of semiconductors<sup>10–12</sup>, but arguably most pronounced, and intensely studied in hydrogenated amorphous silicon (a-Si:H)<sup>13–15</sup>, copper indium–gallium selenide (CIGS)<sup>16–18</sup>, and MHPs<sup>5,8</sup>. In a-Si:H, photoconductivity is observed to fall upon prolonged light-soaking (the Staebler–Wronski Effect)<sup>13</sup>. This behaviour is understood in terms of increased non-radiative recombination occurring via photon-induced meta-stable dangling bonds<sup>15,19</sup>. In CIGS a persistent increase in dark conductance is observed after illumination from white light<sup>18,20</sup>.

Although light-soaking in a-Si:H leads to a reduction in performance, light-soaking often leads to an increase in PCE in MHP-based solar cells<sup>5,8</sup>. A range of hypotheses exist to describe this phenomenon. Light-activated meta-stable states (analogous to those in a-Si:H) is a prevalent description in the literature<sup>6,8</sup>. Interfacial states between the MHP and electron-blocking-layers/hole-blocking-layers also commonly in feature explanations<sup>5,8,21,22</sup>. Other explanations involve the migration of ions leading to internal pin-like structures in the perovskite<sup>7</sup> or a reduction in trap-state density<sup>23,24</sup>. Light-induced halide segregation is a popular description for mixed halide perovskites<sup>4,23,25,26</sup>, in-which optically induced segregation of bromine-rich and iodine-rich regions reduce the overall bandgap in certain compositions (the Hoke Effect)<sup>4</sup>. The fact that changes in photoluminescence yield<sup>27</sup>, diffraction spectra<sup>26</sup>, photoconductance<sup>28</sup>, and absorption coefficient<sup>29</sup> have been observed over periods of seconds to minutes in isolated thin films suggest that the behaviour is at least partially owing to the material itself, rather than interfaces. The theory of light-soaking in MHPs is at present incomplete.

In this report, we employ steady-state microwave conductivity (SSMC)<sup>30–32</sup> to measure the photoconductance of thin films of MHPs under AM1.5 conditions, over a period of many hours. SSMC is a contactless technique (no metallic contacts nor hole-/electron-blocking layers are required to evaluate photoconductance), which does not require large DC electric fields. These features enable us to make statements on the photostability of perovskite compounds themselves, and removes ambiguity arising from interfacial effects<sup>5,8,21</sup> or voltage-induced polarization<sup>33,34</sup>.

## Results

**Photoconductance under white light.** The experimental setup employed in this report is shown diagrammatically in Fig. 1a, and is based upon a similar system developed by the Chabiny Group at the University of California, Santa Barbara<sup>30</sup>. The system is designed to measure thin films of semiconductors on insulators (as depicted in Fig. 1b)<sup>35</sup>. The system can be considered a steady-state analogue of conventional time-resolved microwave conductivity (TRMC)<sup>36</sup>. A standing microwave (~8–9 GHz) electromagnetic field is formed in a waveguide cavity, and a semiconducting sample is positioned at a maximum of the electric-field component of this standing electromagnetic wave. The intensity of microwaves reflected out of the cavity are detected using a Schottky diode and converted to a voltage that is

proportional to microwave intensity. For semiconductors, the carrier density should be low in the dark, and the detected voltage will be constant as a function of time. The closed end of the cavity is made of a transparent conductor (indium tin oxide on glass), through-which the sample is illuminated. With an appropriate bandgap, the incident light generates charge carriers in the film. These carriers move under the influence of the standing electric field, and the reflected microwave intensity (and hence detected voltage) changes upon illumination. With knowledge of the cavity properties one can evaluate how the photoconductance of the film changes from the detected voltage<sup>36</sup> (see Supplementary Note 1 and Supplementary Fig. 1 for details). The approach provides relative (photo-induced) changes in conductance,  $\Delta G$ , and requires a modulated optical source. In conventional TRMC a pulsed laser is normally used<sup>37</sup>. In SSMC, a constant optical illumination source is passed through an optical chopper<sup>30,32</sup>. The measured  $\Delta G$  is evaluated using a lock-in amplifier.

In this report, we study two mixed halide, mixed-cation perovskite films: a double-cation composition:  $\text{FA}_{0.83}\text{Cs}_{0.17}\text{Pb}(\text{I}_{0.9}\text{Br}_{0.1})_3$  (FACs) and a triple-cation composition:  $(\text{FA}_{0.83}\text{MA}_{0.17})_{0.95}\text{Cs}_{0.05}\text{Pb}(\text{I}_{0.9}\text{Br}_{0.1})_3$  (FAMACs), where FA is formamidinium and MA is methylammonium. These compounds were chosen as they are known to lead to high PCEs when employed in solar cells<sup>38,39</sup>, and have been shown to be highly stable in air<sup>40,41</sup>. The later property is particularly valuable as we are measuring electronic properties under illumination, in air, for many hours. The films were prepared on  $0.9\text{ cm} \times 0.9\text{ cm} \times 0.5\text{ mm}$  quartz substrates. The absorption spectra of these two compounds are shown in Fig. 1c, alongside the incident optical spectrum from the solar simulator<sup>42</sup>.

The samples were left in the SSMC cavity in the dark for >1 hour before measurement. The photoconductance of the films was measured as a function of time for 30 minutes before the shutter was opened, after which the photoconductance was measured every 100 ms for a further 18 hours. The samples were fabricated, transported, and stored under inert atmosphere, but were measured unencapsulated in air. The photoconductance as a function of time is shown for FACs and FAMACs in Fig. 2a, b respectively. The samples were illuminated with white (AM1.5) light from a solar simulator. The optical power density was controlled by passing the incident light through neutral density filters. For both compounds, and for optical power densities  $\geq 10\text{ W/cm}^2$ , the conductance is observed to rise over a period of many hours. When illuminated for longer periods of time, the photoconductance of FACs rises sharply for ~12 hours, followed by a slower subsequent rise over 4 days (see Supplementary Note 2 and Supplementary Fig. 2).

The optical power density of commercial solar simulators is known to exhibit small variations as a function of lamp temperature. To rule this out as a potential factor in the increase in  $\Delta G$  as a function of time, the solar simulator was turned on >1 hour prior to measurement in all cases. Supplementary Note 3 describes how the optical power density was monitored as a function of time after the lamp was turned on, as a separate measurement. The results are shown in Supplementary Fig. 3. Although the output does increase for the first 2 minutes, the light source is stable after this time. For this reason, we rule-out instability in lamp output as a contributing factor to the observed increase in  $\Delta G$ .

A similar possible artefact concerns the sample holder temperature, which we address in Supplementary Note 4. In Supplementary Fig. 4 we show the temperature of the sample holder in the cavity measured as a function of time under constant illumination from  $20\text{ mW/cm}^2$  AM1.5 solar spectrum. An increase in cavity temperature of ~1°C is observed upon the first 5 minutes of illumination, followed by an increase of another

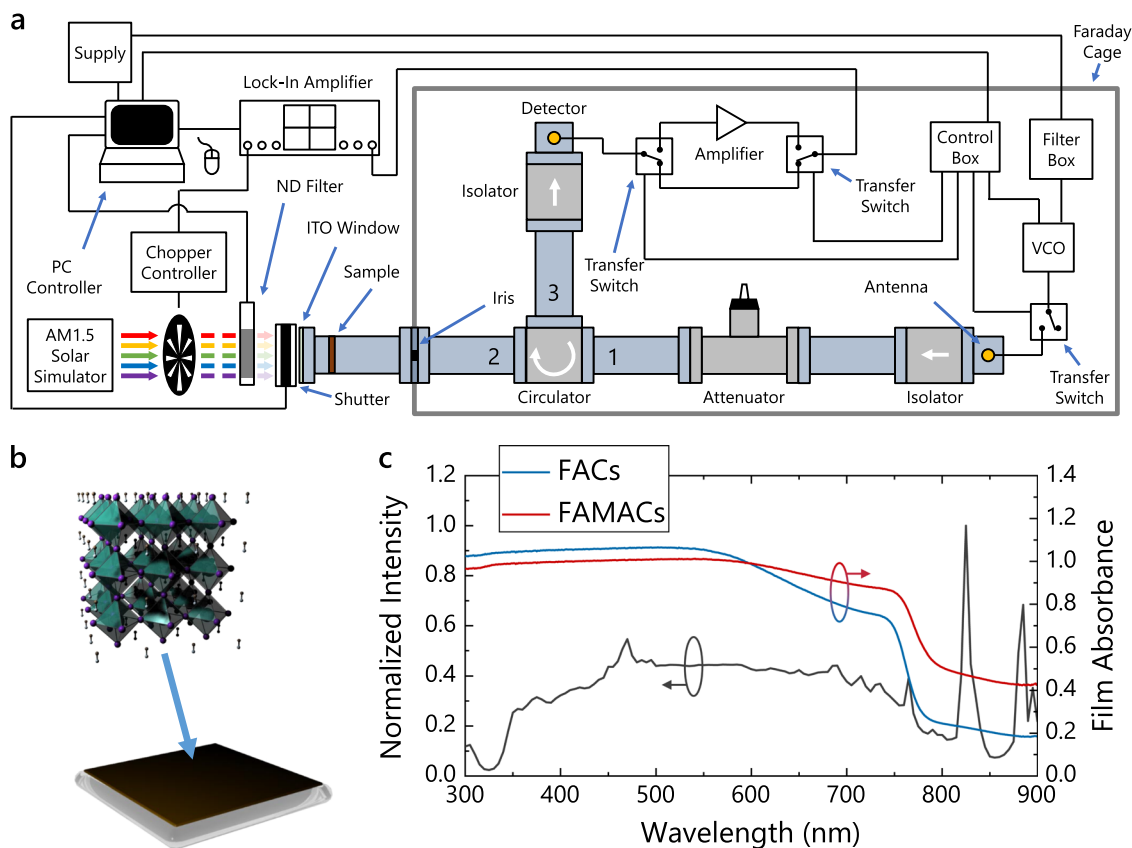


**Fig. 1 Overview of steady-state microwave conductivity measurement strategy.** **a** Schematic diagram of steady-state microwave conductivity (SSMC) system used in this study. Abbreviations are as follows: PC personal computer, AM air mass, ND neutral density, ITO indium tin oxide, VCO voltage-controlled oscillator. **b** Schematic illustrating that films are simply solution-processed metal halide perovskite (MHP) on quartz. The crystal structure shown is that of (MA)PbI<sub>3</sub> but is meant to be illustrative of the samples employed. Purple spheres represent iodine atoms, green octahedra surround lead atoms, brown spheres represent carbon atoms, and grey spheres represent nitrogen atoms. Hydrogen atoms in (MA) are omitted for clarity. **c** Normalised intensity of light incident on sample, provided by manufacturer<sup>42</sup>, with absorbance of FA<sub>0.83</sub>CS<sub>0.17</sub>Pb(I<sub>0.9</sub>Br<sub>0.1</sub>)<sub>3</sub> (FACs) and (FA<sub>0.83</sub>MA<sub>0.17</sub>)<sub>0.95</sub>CS<sub>0.05</sub>Pb(I<sub>0.9</sub>Br<sub>0.1</sub>)<sub>3</sub> (FAMACs) films. MA methylammonium, FA formamidinium. Figure 1a Adapted with permission from ref. <sup>35</sup>. Copyright (2019) American Chemical Society.

~1°C, over the subsequent 12 hours. An increase in temperature of 2°C is not expected to affect carrier mobility, and hence conductance, significantly. The mobility of charge carriers in thin films of MHPs are generally observed to be inversely correlated with temperature<sup>43</sup>. As we observe an increase in conductance as a function of time, it is hence reasonable to conclude that changes in  $\Delta G$  are unlikely to be owing to changes in cavity temperature.

Given the reasons described in the preceding two paragraphs, we interpret the increase in conductance observed in Fig. 2a, b in terms of photo-induced instabilities of the perovskite; consistent with previous observations of the light-soaking effect in the literature<sup>5,7,8,25</sup>. It has previously been shown<sup>30</sup> that values of  $\Delta G$  measured from SSMC measurements can be used to evaluate a proxy for the mobility-lifetime product:  $\phi\Sigma\mu\tau$ , as defined by Eq. 1.

$$\phi\Sigma\mu\tau = \phi(\tau_e\mu_e + \tau_h\mu_h) \quad (1)$$

$\mu_e$  and  $\mu_h$  are the average electron and hole mobilities measured over the sample area, respectively.  $\tau_e$  and  $\tau_h$  are representative electron and hole lifetimes, respectively. Here  $\phi$  is the carrier-generation efficiency, i.e., the number of electron-hole pairs generated per absorbed photon ( $\phi \in [0, 1]$ ). In materials with low exciton binding energies, such as MHPs<sup>44</sup>, one can assume that  $\phi \approx 1$  and hence interpret  $\phi\Sigma\mu\tau \approx \mu_e\tau_e + \mu_h\tau_h$ .  $\phi\Sigma\mu\tau$  has the same units as mobility-lifetime product, but carrier-specific information is obscured. The derivation of  $\phi\Sigma\mu\tau$  is described in Supplementary Note 5 and previous work<sup>30</sup>. The derivation of  $\phi\Sigma\mu\tau$  assumes that the semiconductor is in steady state at the

end of each illumination cycle. We validate this assumption for a chopper frequency of 4 kHz in Supplementary Note 6 and Supplementary Fig. 5.  $\phi\Sigma\mu\tau$  as a function of time under illumination is shown for FACs and FAMACs in Fig. 2c, d, respectively.

**Time-resolved microwave conductivity measurements.** With  $\phi$  assumed to be very close to unity in these compounds, the question remains as to the relative contributions of mobility and lifetime to  $\phi\Sigma\mu\tau$ . It is reasonable to expect that optically pre-filling traps or lower-energy transport states could affect average mobility. To help address this question, conventional TRMC measurements were carried out on an FACs sample with and without background illumination from AM1.5 illumination. A schematic diagram of the TRMC system employed is shown in Fig. 3a. The TRMC and SSMC systems used in this study are modified versions of the same apparatus<sup>35,37</sup>. TRMC is an established technique<sup>36</sup>, for measuring the photoconductance of a film upon excitation from a pulsed (~nanosecond) laser. Further analysis<sup>36</sup> allows one to evaluate a proxy for mobility:  $\phi\Sigma\mu$ , as given by Eq. 2:

$$\phi\Sigma\mu = \phi(\mu_e + \mu_h) \quad (2)$$

Conventionally, TRMC measurements are carried out on-resonance, and changes in detector voltage are implicitly assumed to be owing to real changes in conductance. However, by carrying

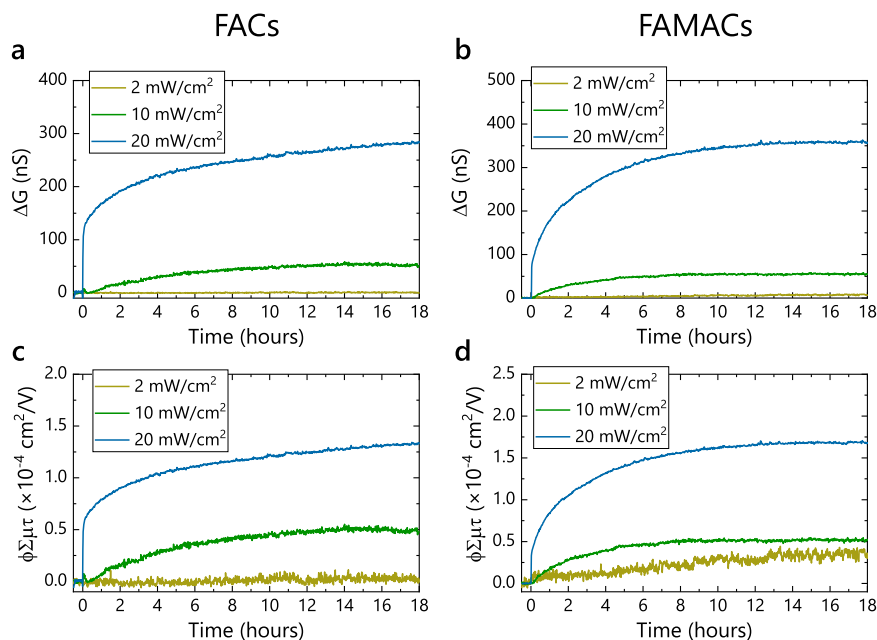


**Fig. 2 Time-dependent photoconductance of metal halide perovskite films.** **a, b** Photoconductance,  $\Delta G$ , of **a**,  $\text{FA}_{0.83}\text{Cs}_{0.17}\text{Pb}(\text{I}_{0.9}\text{Br}_{0.1})_3$  (FACs) and **b**,  $(\text{FA}_{0.83}\text{MA}_{0.17})_{0.95}\text{Cs}_{0.05}\text{Pb}(\text{I}_{0.9}\text{Br}_{0.1})_3$  (FAMACs) measured as a function of illumination time, under constant AM1.5 optical illumination, at various intensities. **c, d**  $\phi\Sigma\mu\tau$  of **c**, (FACs) and **d**, (FAMACs) extracted from  $\Delta G$ , as a function of illumination time, under constant AM1.5 optical illumination, for various illumination intensities.  $\phi\Sigma\mu\tau = \phi(\tau_e\mu_e + \tau_h\mu_h)$ , where  $\mu_e$  and  $\mu_h$  are the average electron and hole mobilities measured over the sample area, respectively.  $\tau_e$  and  $\tau_h$  are representative electron and hole lifetimes, respectively. Here  $\phi$  is the carrier-generation efficiency, i.e., the number of electron-hole pairs generated per absorbed photon ( $\phi \in [0, 1]$ ). All measurements were carried out at room temperature in air using the steady-state microwave conductivity (SSMC) system shown in Fig. 1. The same samples were measured in order of increasing optical power density, and were stored in inert atmosphere  $\text{N}_2$ , in the dark for at least 24 hours between experiments.

out measurements as a function of microwave frequency, it has been shown that it is possible to resolve real ( $\Delta G \equiv \Delta G'$ ) and imaginary ( $\Delta G''$ ) components of conductance<sup>45</sup>. The extraction and evaluation of  $\Delta G'$  and  $\Delta G''$  is described in Supplementary Note 7, and we here just consider the real photoconductance:  $\Delta G'$  (i.e., the contribution owing to free carriers only). As depicted in Fig. 3a, we here use a beam splitter to mix AM1.5 constant (unchopped) illumination with a  $\sim 5$  ns 532 nm pulse from a Nd:YAG laser. The optical power density incident on the sample owing to the solar simulator was  $10 \text{ mW/cm}^2$ . Example TRMC transients ( $\Delta G'$  as a function of time) are shown in Supplementary Fig. 6 for an FACS sample before, during, and after illumination from  $10 \text{ mW/cm}^2$  AM1.5 light. The purpose of this TRMC experiment is to not study light-soaking directly<sup>28</sup>, but to elucidate what effect, if any, background illumination has on carrier mobility.

Figure 3b shows the TRMC figure of merit ( $\phi\Sigma\mu$ ) extracted from the real photoconductance as a function of laser fluence, before, during, and after illumination from  $10 \text{ mW/cm}^2$  AM1.5 light. At high laser fluence, a significant amount of bimolecular and Auger recombination will occur during the  $\sim 5$  ns laser pulse, resulting in a reduction in peak observable photoconductance, and hence a reduction in extracted  $\phi\Sigma\mu$  (as observed in Fig. 3b). This is a widely observed phenomenon in TRMC, and models have been developed to account for it<sup>46</sup>. By applying such a model<sup>46</sup>, we approximate representative values of  $\phi\Sigma\mu$ , as shown in Fig. 3c. Although TRMC is known to underestimate mobilities in certain cases<sup>47</sup>, relative measurements are generally unambiguous. It is clear from the data presented in Fig. 3 that illumination at  $10 \text{ mW/cm}^2$  appears to have no significant impact on the average measured mobility of free charge. This result suggests that the changes in  $\phi\Sigma\mu\tau$  occurring over many hours, shown in Fig. 2, are unlikely to be owing to an enhancement in average mobility alone.

The recovery of photoconductance was investigated in Supplementary Note 8, Supplementary Figs. 7 and 8. An FACS sample was illuminated with  $10 \text{ mW/cm}^2$  AM1.5 illumination for 12 hours, then left in the dark for 12 hours, before being illuminated again with AM1.5 illumination for a further 12 hours (Supplementary Fig. 8). Immediately after the shutter is initially opened (time = 0) the photoconductance rises to  $\sim 350$  nS, before increasing to  $\Delta G \approx 675$  nS during the subsequent 12 hours of illumination. When the shutter is closed, the measured photoconductance drops to zero. When the shutter is opened for the second time (after a total of 24 hours), the photoconductance partially recovers to around 500 nS. After another 12 hours of light soaking, the photoconductance eventually reaches a peak value of  $\Delta G \approx 700$  nS. The data suggest the process is, at least partially, reversible.

**Photoconductance under green light.** To probe whether photo-induced changes in bandgap<sup>4</sup>, and hence changes in the fraction of photons absorbed, are responsible for the observed light soaking, samples were also measured with above bandgap light from a green light-emitting diode (LED), with a peak emission wavelength of 525 nm. Figure 4a shows the photoconductance of thin films of FACS and FAMACs measured using SSMC, under illumination from green light at  $10 \text{ mW/cm}^2$ . Figure 4a demonstrates that these samples exhibit the light soaking effect under monochromatic light, and it is hence unlikely that photo-induced changes in optical bandgap are the only relevant process. The most striking difference between SSMC data acquired under white and green light is the magnitude of photoconductance, which is roughly an order of magnitude higher under green light for both FACS and FAMACs. The spectrum-integrated optical power density is  $10 \text{ mW/cm}^2$  for each source, so the percentage of

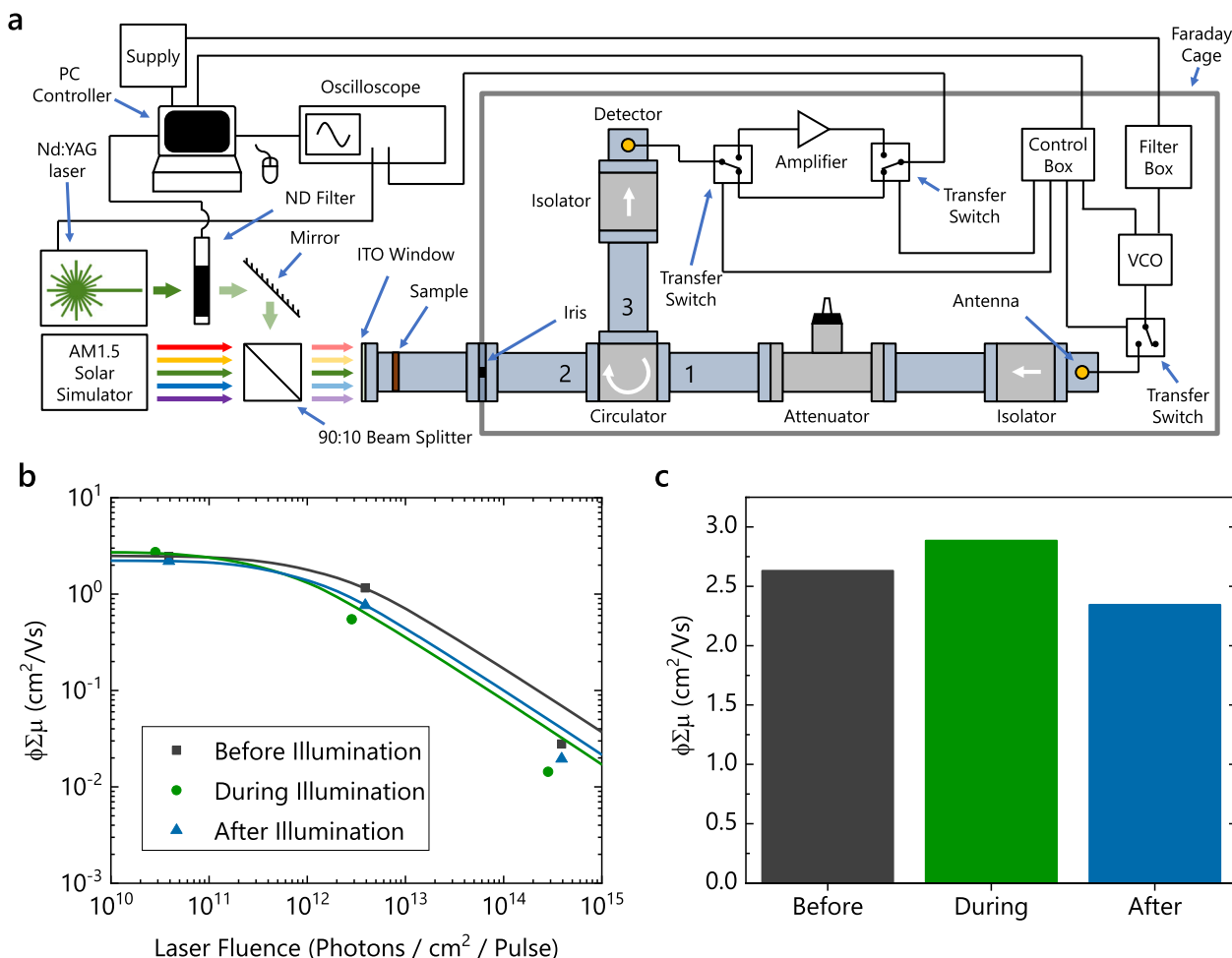


**Fig. 3 Time-resolved microwave conductivity measurements.** **a** Schematic diagram of time-resolved microwave conductivity system (TRMC) used in this study. This setup is a modified version of the steady-state microwave conductivity (SSMC) apparatus depicted in Fig. 1. Abbreviations are as follows: PC personal computer, AM: air mass, ND neutral density, ITO indium tin oxide, VCO voltage-controlled oscillator, Nd:YAG neodymium-doped yttrium aluminium garnet. **b**  $\phi \Sigma \mu = \phi(\mu_e + \mu_h)$  of  $\text{FA}_{0.83}\text{Cs}_{0.17}\text{Pb}(\text{I}_{0.9}\text{Br}_{0.1})_3$  (FACs) film extracted from real conductance, as a function of laser fluence before, during, and after illumination.  $\mu_e$  and  $\mu_h$  are the average electron and hole mobilities measured over the sample area, respectively.  $\phi$  is the carrier-generation efficiency, i.e., the number of electron-hole pairs generated per absorbed photon ( $\phi \in [0, 1]$ ). The points are experimental values and the lines are fits to a numerical model<sup>46</sup> accounting for bimolecular and Auger recombination during the laser pulse. **c** Representative values of  $\phi \Sigma \mu$  of FACs film before, during, and after illumination, extracted from the numerical fits in **b**. All measurements were carried out at room temperature in air. Figure 3a Adapted with permission from ref. 35. Copyright (2019) American Chemical Society.

above-gap photons will be higher for the green light source. This difference alone however can only account for a  $\sim 2$ – $3$ -fold increase in  $\Delta G$  (calculation not shown) not a factor of  $\sim 10$ . Previous reports<sup>48</sup> have illustrated that the differences in excitation wavelength can lead to distinct light-soaking phenomena. For this reason, we interpret the results presented in Figs. 2 and 4a as being evidence that light soaking under white light is due to multiple, competing, processes.

The values of  $\Delta G$  obtained from SSMC data are owing to photo-induced charge carriers only, and do not enable us to comment on changes in background conductance. For this reason we carried out simple two-terminal device measurements<sup>49</sup> of a thin film of FAMACs under illumination. Figure 4b shows the conductance  $G$ , (i.e., sum of both background and photogenerated conductance) of an FAMACs film measured for  $\sim 90$  minutes in the dark, before being illuminated with green light (peak 525 nm) at an intensity of  $10 \text{ mW/cm}^2$  for 10 hours. After illumination, the device was held in the dark for a further 10 hours. A bias of 2 V was continually applied throughout the measurement. The electrodes were gold and the channel length

was  $10 \mu\text{m}$ . Upon application of the voltage in the dark, the current increases for  $\sim 30$  minutes, before stabilizing. Upon illumination, an initial spike in  $G$  is observed, after which the conductance slowly falls over the subsequent 10 hours. After the light is removed, the film retains a conductance  $\sim 25$ – $35$  times higher than its pre-illumination value. The same data are plotted with a linear  $y$  axis scale in Supplementary Note 9 and Supplementary Fig. 9.

The reduction in total conductance ( $G$ ) as shown in Fig. 4b is, on first inspection, contradictory to the observed increase in photoconductance ( $\Delta G$ ) observed in the SSMC measurements (e.g., Fig. 4a). We believe the observed reduction in  $G$  is likely to be owing to either the presence of injecting electrodes, the  $\text{SiO}_2/\text{MHP}$  interface, and/or the constant DC bias. The ionic polarizability<sup>34</sup> of MHPs is believed to screen electronic charge at room temperature, and has led to difficulties in demonstrating field-effect devices based on MHPs<sup>50,51</sup>. In addition, extended illumination in other material systems is known to lead to a photo-gating affect<sup>52</sup>, resulting in a shift of the threshold voltage in thin-film transistors. A positive shift in threshold voltage under

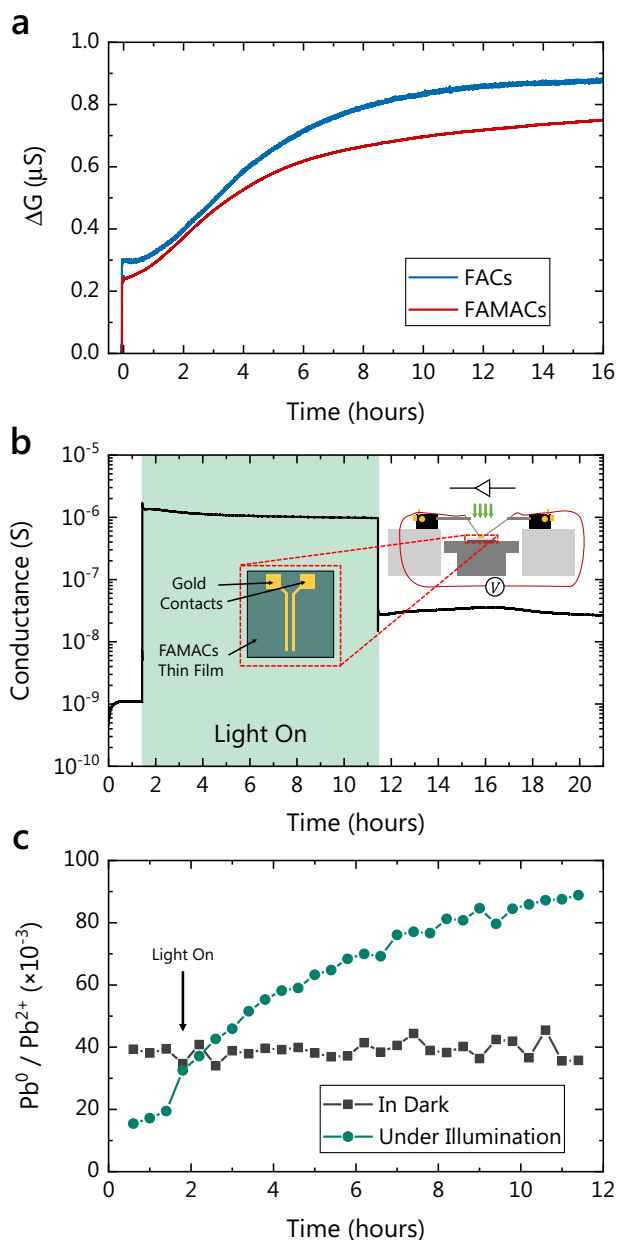


**Fig. 4 Behaviour under illumination from green light.** **a** Photoconductance,  $\Delta G$ , of isolated thin films of  $\text{FA}_{0.83}\text{Cs}_{0.17}\text{Pb}(\text{I}_{0.9}\text{Br}_{0.1})_3$  (FACs) and  $(\text{FA}_{0.83}\text{MA}_{0.17})_{0.95}\text{Cs}_{0.05}\text{Pb}(\text{I}_{0.9}\text{Br}_{0.1})_3$  (FAMACs) on quartz, measured as a function of illumination time, under constant optical illumination from green light-emitting diode with peak emission wavelength of 525 nm at 10 mW/cm<sup>2</sup>, using steady-state microwave conductivity (SSMC). **b** Conductance of FAMACs measured using before, during, and after illumination from green light (525 nm) at an optical power density of ~10 mW/cm<sup>2</sup>. Conductance was in this case measured with a two-terminal device structure consisting of SiO<sub>2</sub> (230 nm) on Si surface, with gold electrodes. The electrodes had a separation of 10  $\mu\text{m}$  and a width of 10 mm. The Si surface was grounded for this measurement. Inset: simplified schematic diagram illustrating experimental setup for this measurement. **c** Ratio of metallic Pb<sup>0</sup> to Pb<sup>2+</sup> in FAMACs thin film, measured as a function of time using X-ray photoelectron spectroscopy (XPS). XPS measurements were carried out separately on two identically processed thin films, one under illumination from green light (525 nm) at an optical power density of ~10 mW/cm<sup>2</sup>. SSMC measurements were carried out in air, two-terminal device measurements were carried out under ambient pressure N<sub>2</sub>, and XPS measurements were carried out under high ( $3 \times 10^{-10}$  mbar) vacuum.

illumination would be manifest as a lower current at zero gate voltage (i.e., what we have in our two-terminal measurements). Combined, these contributions make it challenging to isolate a single mechanism for the decrease in  $G$  over the period of illumination, and indeed illustrate why contactless measurements can in certain situations provide less ambiguity. For this reason, we do not strongly advocate a single process for the decrease in  $G$  observed during illumination. We instead focus on the fact that the film retains an increased conductance after illumination. Because the conductance was stable before illumination, we can say unambiguously that extended illumination has resulted in a persistent background conductance.

Persistent photoconductivity as observed in Fig. 4b is reminiscent of a similar effect observed in CIGS systems<sup>20</sup>, which has previously been attributed to light-induced vacancy formation<sup>53,54</sup>. To study this possibility in our systems, we carried out X-ray photoemission spectroscopy (XPS) on films of FAMACs on quartz. Figure 4c shows the ratio of metallic Pb<sup>0</sup> to Pb<sup>2+</sup> of two FAMACs samples, measured over period of 12 hours, one in the dark and another under illumination from green light with an approximate intensity of 10 mW/cm<sup>2</sup>, as separate experiments. The relative content of other relevant atomic species (e.g., Cs, N, C, I) were observed to be roughly constant as a function of time—see Supplementary Note 10 and Supplementary Fig. 10. Although the conversion of Pb<sup>2+</sup> to Pb<sup>0</sup> is consistent with our observation of increased background conductance after illumination (Fig. 4b), it is currently unclear why this would lead to an increase in photoconductance (e.g., Fig. 2). We acknowledge the nature of photogenerated defects is a complex issue in mixed halide systems<sup>55</sup>, and that further experiments are required.

The formation of metallic lead upon illumination has previously been observed via XPS<sup>56</sup> in methylammonium lead iodide ((MA)PbI<sub>3</sub>), and has been suggested to occur via (MA)PbI<sub>3</sub> degradation into PbI<sub>2</sub><sup>57</sup>, which is itself known to decompose under illumination and heat into Pb and I<sub>2</sub><sup>58</sup>. To rule out any irreversible changes in structure owing to illumination, we carried out X-ray diffraction before and after light soaking under AM1.5 spectra (see Supplementary Note 11 and Supplementary Fig. 11). FACs and FAMACs samples were illuminated at 10 mW/cm<sup>2</sup> or 40 mW/cm<sup>2</sup> for 18 hours, then were stored in the dark in N<sub>2</sub> > 1 week. Although we do observe a PbI<sub>2</sub> impurity in all FAMACs films (including pristine films), no significant changes in structure were observed between pristine samples and those exposed to illumination. We hence conclude that the structure is largely unaffected by light soaking at these intensities and for these durations. As we also observe light-soaking to be, at least partially, reversible (see Supplementary Fig. 8), we do not attribute our observations to an irreversible degradation of the perovskite to a lower-dimensional structure.

## Discussion

Although extended illumination of MHPs often results in an increased photoconductance, in a-Si:H extended illumination is known to cause a reduction in photoconductance<sup>13,15,19</sup>. It is noteworthy that descriptions of changes in photoconductance in a-Si:H are similar, phenomenologically, to those used to describe voltage-induced bias-stress behaviour in a-Si:H thin-film transistors (TFTs):<sup>59</sup> extended application of a gate voltage leads to the creation of reversible trap states, an increase in persistent charge, and a subsequent change in threshold voltage. The threshold voltage (and hence interface trap concentration) in TFTs is often modelled with a (quasi-empirical) stretched-exponential function<sup>60–62</sup>. An analogous stretched-exponential

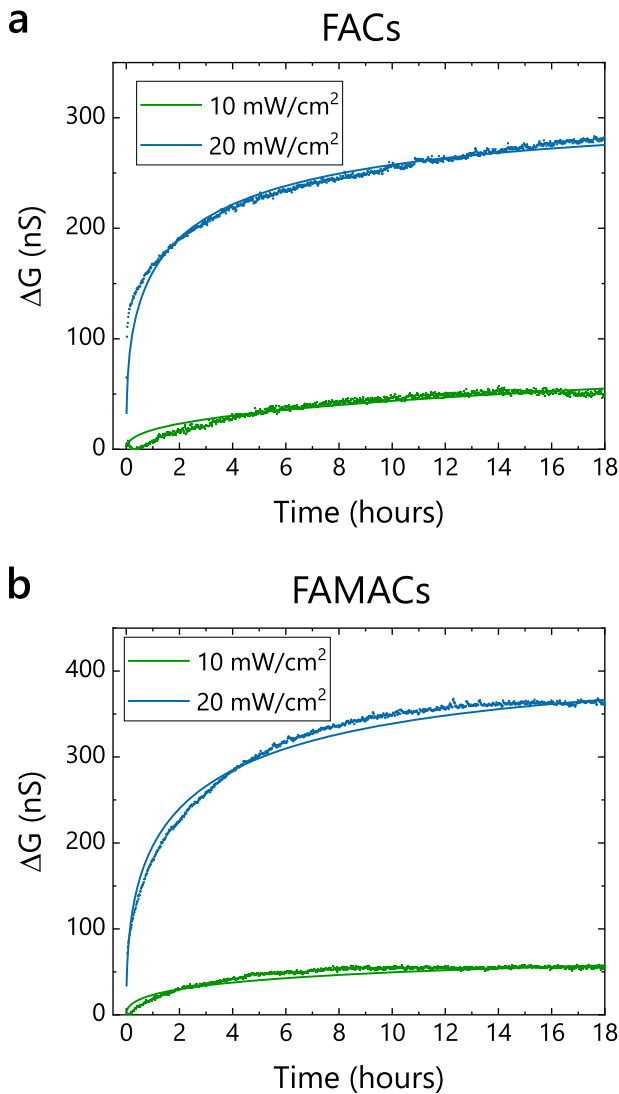


**Fig. 5 Photoconductance fitted to stretched-exponential function.** Photoconductance,  $\Delta G$ , of **a**  $\text{FA}_{0.83}\text{CS}_{0.17}\text{Pb}(\text{I}_{0.9}\text{Br}_{0.1})_3$  (FACs), and **b**  $(\text{FA}_{0.83}\text{MA}_{0.17})_{0.95}\text{CS}_{0.05}\text{Pb}(\text{I}_{0.9}\text{Br}_{0.1})_3$  (FAMACS) measured as a function of illumination time, under constant AM1.5 optical illumination at 10 and 20  $\text{mW}/\text{cm}^2$  (points). The lines are fits to the stretched-exponential function given by Eqs. (3) and (5). From these fits we obtain values of  $\beta = 0.40$  and  $E_A = 0.77$  eV for FACs, and  $\beta = 0.44$  and  $E_A = 0.77$  eV for FAMACS.

equation for photoconductance is given by Eq. 3:

$$\Delta G(t) = \Delta G_0 \left( 1 - \exp \left[ - \left( \frac{t}{\tau} \right)^\beta \right] \right) \quad (3)$$

Where  $t$  is the time under illumination, and  $\Delta G_0$  is the photoconductance as  $t \rightarrow \infty$ .  $\beta$  is the dimensionless dispersion parameter, defined by Eq. 4:

$$\beta = \frac{T}{T_0} \quad (4)$$

$T$  is temperature, and  $T_0$  is the characteristic trap-state width (units of temperature) of the material. The parameter  $\tau$  is the temperature-activated relaxation-time, and is given by Eq. 5:

$$\tau = \nu^{-1} \exp \left( \frac{E_A}{k_B T} \right) \quad (5)$$

$E_A$  is the mean activation energy for trap formation,  $k_B$  is the Boltzmann Constant, and  $\nu$  is the trap-formation attempt-frequency. It is reasonable to assume that  $\beta$  and  $E_A$  are material properties (i.e., independent of illumination intensity), whereas  $\nu$  and  $\Delta G_0$  are both dependent on illumination intensity.

Figure 5 shows Eqs. 3 and 5 fitted to the time-dependent photoconductance of FACs and FAMACS, under illumination from 10  $\text{mW}/\text{cm}^2$  and 20  $\text{mW}/\text{cm}^2$  white light. For each material,  $\beta$  and  $E_A$  were forced to be independent of light intensity, whereas  $\nu$  and  $\Delta G_0$  could vary as a function of intensity. From these fits, we obtain values of  $\beta = 0.40$  and  $E_A = 0.77$  eV for FACs and  $\beta = 0.44$  and  $E_A = 0.77$  eV for FAMACS. From past TFT voltage-induced bias-stress measurements, typical room temperature values of  $\beta = 0.4$ – $0.6$  and  $E_A = 0.9$ – $1.0$  eV have been reported for a-Si<sup>63,64</sup>,  $\beta = 0.4$ – $0.5$  and  $E_A = 0.5$ – $0.6$  eV for amorphous indium–gallium–zinc oxide (IGZO)<sup>62</sup>, and  $\beta = 0.44$  and  $E_A = 0.5$ – $0.6$  eV for organic semiconductors<sup>65</sup>.

Although empirical, using a stretched exponential to describe light soaking is not an unreasonable approach. There are known similarities between the application of extended illumination and application of extended gate voltages in a-Si:H systems<sup>15,60</sup>. Given that bias stressing is routinely observed to occur over periods of multiple hours<sup>66</sup>, it is also conceivable that extended illumination leads to generation and/or removal of persistent trap states over similar timescales. Similarly, the large absorption coefficients in MHPs suggest an inhomogeneous vertical distribution of charge, reminiscent of charge distributions in TFTs, will be produced under constant illumination<sup>67</sup>. Although further study (including temperature-dependent measurements, wavelength-dependent measurements, composition-dependent measurements, and hole- and electron-resolved parameters) is clearly needed to elucidate the details of this phenomenon, it is hoped the data presented here will guide future experiments in the endeavour of resolving the light-soaking effect.

In conclusion, we have used SSMC to probe the time-dependent photoconductance of metal halide perovskites. By illuminating isolated thin films of two mixed halide, mixed-cation perovskites with AM1.5 solar illumination, we observe a continual increase in photoconductance over a period of 18 hours. As our technique is contactless, these results illustrate how light soaking cannot exclusively be an interfacial effect, nor an effect owing to DC external fields alone. By applying time-resolved microwave conductivity to films under illumination from AM1.5 illumination at an incident power density of 10  $\text{mW}/\text{cm}^2$ , we also rule out changes in average carrier mobility as being a dominant mechanism. The mechanisms responsible for this observation remain unresolved but are likely owing to multiple competing factors. We are able to fit the observed changes in photoconductance to a quasi-empirical stretched-exponential function, in an analogous manner to bias-stressed TFTs. The information provided in this report should help the community better understand one of the most perplexing open problems in the field of perovskite solar cells and, ultimately, lead to more robust and predictable devices.

## Methods

**Sample preparation.** Lead iodide ( $\text{PbI}_2$ , 99.999%, metals basis) was purchased from Alfa-Aesar and lead bromide ( $\text{PbBr}_2$ ,  $\geq 98\%$ ) from Alfa-Aesar. Cesium iodide ( $\text{CsI}$ , 99.99%) was purchased from Alfa-Aesar. Formamidinium iodide (FAI) and methylammonium iodide (MAI) were purchased from GreatCell Solar. To form the mixed-cation lead mixed-anion perovskite precursor solutions,  $\text{CsI}$ , FAI,  $\text{PbI}_2$ , and  $\text{PbBr}_2$  were prepared in the way corresponding to the exact stoichiometry for the desired metal halide perovskite composition in a mixed organic solvent system comprising anhydrous  $N,N$ -dimethylformamide (DMF) and anhydrous dimethyl sulfoxide (DMSO) at the ratio of DMF:DMSO = 4:1. The perovskite precursor concentration used was 1.45 M. The deposition of the mixed-cation lead mixed-anion perovskite layers was carried out using a spin coater in a nitrogen-filled glove

box with the following processing parameters: starting at 1000 rpm for 5 sec (ramping time of 5 sec from stationary status) and then 5000 rpm (ramping time of 5 sec from 1000 rpm) for 30 sec. Before the end of the spinning process, a solvent-quenching method<sup>68</sup> was used by dropping 300- $\mu$ L anisole onto the spinning substrates at 40 sec after the start of the spin-coating process. The thermal annealing process (100 °C for 50–60 min) was then carried out for the formation of the perovskite layer.

**Ultraviolet-visible spectroscopy.** The ultraviolet-visible (UV-Vis) transmission measurements were performed using a Shimadzu UV-2600 UV-Vis spectrophotometer. The measurements were carried in air at room temperature.

**SSMC experiments.** A schematic representation of the SSMC system employed in this study is shown in Fig. 1a<sup>35</sup>. This SSMC system is home-built and based on similar systems employed at the University of California, Santa Barbara<sup>30</sup> and the National Renewable Energy Laboratory<sup>32</sup>. A microwave frequency oscillatory electric signal is generated using a Sivers IMA VO4280X/00 voltage-controlled oscillator (VCO). The signal has an approximate power of 16 dBm and a tunable frequency between 8 GHz and 15 GHz. The VCO is powered with an NNS1512 TDK-Lambda constant 12 V power supply, and the output frequency is controlled by a Stahl Electronics BSA-Series voltage source. Both the power supply and tuning voltage are filtered by a combination of active and passive filters before being supplied to the VCO. The oscillatory signal is incident on an antenna inside a WR90 copper-alloy waveguide. The microwaves emitted from the antenna pass through an isolator and an attenuator before they are incident on a circulator (Microwave Communication Laboratory Inc. CSW-3). The circulator acts as uni-directional device in which signals entering from port 1 exit through port 2 and signals entering from port 2 exit through port 3. The incident microwaves pass through a fixed iris (6.35 mm diameter) into a sample cavity. The cavity supports a TE<sub>102</sub> mode standing wave and consists of an ITO-coated glass window that allows optical access to the sample. The sample is mounted inside the cavity at a maximum of the electric-field component of the standing microwaves, using a 3D-printed PLA sample holder. Microwaves reflected from the cavity are then incident on port 2 of the circulator, exiting through port 3, directed through an isolator, and onto a zero-bias Schottky diode detector (Fairview Microwave SMD0218). The detector outputs a voltage which is linearly proportional to the amplitude of the incident microwaves. The amplifier depicted in Fig. 1a is bypassed in SSMC measurements using two computer controlled Mini-Circuits MTS-18-12B+ transfer switches. An Oriol LCS-100 solar simulator or a Thorlabs SOLIS-525C high power green LED was used to illuminate the sample. The solar simulator was turned on >1 hour before all SSMC measurements carried out. Light was passed through a Stanford Research Systems SR540 optical chopper operating at 4 kHz for all measurements. The chopped light was passed through a range of neutral density filters before being incident on a computer controlled ThorLabs SH1 Optical Beam Shutter. The optical power density was measured to be ~0 mW/cm<sup>2</sup> when the beam obscured by a chopper blade in all cases, and incident optical power density was measured when unobscured by chopper blades. The incident optical power density was measured using a Newport 919P-003-10 high sensitivity thermopile sensor and a Newport 1936-R Power Meter. The sample was left in the dark for 30 minutes before the shutter was opened, and the measurement then continued for a further 18 hours. The peak-to-peak detector voltage was measured, unamplified, using a Stanford Research Systems SR865 lock-in amplifier, in phase-locked mode. The voltage was sampled every 100 ms, then binned into 1-minute intervals in order to improve the signal-to-noise ratio. The photoconductance was evaluated from the peak-to-peak voltage as described in Supplementary Note 1. The proxy for mobility-lifetime product ( $\phi\Sigma\mu\tau$ ) was approximated from photoconductance, incident optical power density and sample absorption, as described in Supplementary Note 5.

**Time-resolved microwave conductivity experiments.** A schematic representation of the TRMC system employed here is depicted in Fig. 3a. This is a modified version of the SSMC system depicted in Fig. 1a, and is very similar to the system as described previously<sup>37</sup>. Unlike the SSMC experiment, in the TRMC experiment the detected voltage signal is amplified by a Femto HAS-X-1-40 high-speed amplifier (gain =  $\times 100$ ). The amplified detector voltage is measured as a function of time by a Tektronix TDS 3032 C digital oscilloscope. Instead of using a solar simulator and an optical chopper, a Continuum Minilite II pulsed Nd:Yag laser is used to illuminate the sample. The laser pulse has a wavelength of 532 nm, a full width at half-maxima of ~5 ns and a maximum fluence incident on the sample of ~10<sup>15</sup> photons/cm<sup>2</sup>/pulse. An external trigger link is employed to trigger the oscilloscope before the laser fires. The real photoconductance, imaginary photoconductance, and TRMC figure of merit ( $\phi\Sigma\mu$ ) are extracted from the detected voltage as described in Supplementary Note 7. In order to study the effect of background illumination on  $\phi\Sigma\mu$ , the sample was exposed to continuous illumination from AM1.5 solar illumination, whereas the conventional TRMC experiment was taking place. The AM1.5 illumination was mixed with that from the pulsed laser using a 90:10 beam splitter. The power density incident on the sample from the AM1.5 solar spectrum was 10 mW/cm<sup>2</sup>.

**X-Ray diffraction.** X-ray diffraction (XRD) patterns were obtained with an X-ray diffractometer (D8-Discover, Bruker) using Cu K $\alpha$  x-ray source ( $\lambda = 1.541 \text{ \AA}$ ).

**Two-terminal device measurements.** Pre-patterned bottom-gate, bottom-contact transistor substrates were purchased from Fraunhofer IPMS. Substrates consisted of highly n-doped silicon ( $n \approx 3 \times 10^{17} \text{ m}^{-3}$ ) wafers with thermally grown 230 nm SiO<sub>2</sub> insulating layer. Source and drain electrodes 30 nm-thick Au on a 10 nm adhesion layer of indium tin oxide. The channel length of the device measured was 10  $\mu$ m and the device width 10 mm. The FAMACs film was deposited onto the pre-patterned substrate following an identical procedure used for films deposited on quartz substrates. Two-terminal device measurements were carried out using an Everbeing C-2 probe station and a Keithley 2400 sourcemeter controlled by a PC via a general-purpose interface bus interface. The common gate electrode was grounded and the source-drain voltage was 2 V for all measurements. The two-terminal measurements were carried out in N<sub>2</sub> at ambient pressure.

**X-ray photoelectron spectroscopy.** X-ray photoelectron spectroscopy measurements were conducted in a custom-built near-ambient pressure system from SPECS Surface Nano Analysis GmbH using monochromatized Al K $\alpha$  radiation ( $h\nu = 1486.6 \text{ eV}$ , 50 W, 15 kV) under ultra-high vacuum condition ( $3 \times 10^{-10}$  mbar). The electron analyzer pass energy was set to 35 eV and normal emission was used with an analytical spot size of ~300  $\mu$ m. Two FAMACs samples were studied with and without illumination from green light (maximum emission 525 nm) through a view port on the XPS chamber. To compensate the charging effect, a flood gun with low energy electron energy of 0.2 eV with currents set to 0.6 and 0.8  $\mu$ A for samples measured with light source On and Off, respectively. The XPS data were charge corrected to the C 1 s aliphatic carbon binding energy ( $E_b$ ) at 284.8 eV<sup>69</sup>. The surface chemistry was investigated by collecting XPS data (non-stop) for an extended period up to 12 hours. XPS core levels of Pb 4f, Cs 3d, I 3d, C 1 s, and N 1 s were recorded with an energy step size of 0.1 eV. All spectra were fit by CasaXPS software using Gaussian-Lorentzian line shapes with a linear background. The atomic ratios  $R$  of the samples were obtained using Eq. 6 adapted from Physical Electronics (Perkin Elmer)<sup>69</sup>. Values of the corresponding atomic sensitivity factors  $S$  are based on the peak area measurements obtained from empirical data<sup>70</sup> and values for  $I$ , which is the number of photoelectrons per second to scale the measured areas in a specific spectra peak computed from the corresponding fitted spectra using CasaXPS.

$$R = \frac{I_x/S_x}{I_y/S_y} \quad (6)$$

## Data availability

The data sets generated during and/or analysed during the current study are available from the corresponding author upon reasonable request.

Received: 12 July 2019; Accepted: 6 April 2020;

Published online: 30 April 2020

## References

- Jena, A. K., Kulkarni, A. & Miyasaka, T. Halide perovskite photovoltaics: background, status, and future prospects. *Chem. Rev.* **119**, 3036–3103 (2019).
- Nelson, J. Polymer:fullerene bulk heterojunction solar cells. *Mater. Today* **14**, 462–470 (2011).
- Battaglia, C., Cuevas, A. & De Wolf, S. High-efficiency crystalline silicon solar cells: status and perspectives. *Energy Environ. Sci.* **9**, 1552–1576 (2016).
- Hoke, E. et al. Reversible photo-induced trap formation in mixed-halide hybrid perovskites for photovoltaics. *Chem. Sci.* **6**, 613–617 (2015).
- Zhao, C. et al. Revealing underlying processes involved in light soaking effects and hysteresis phenomena in perovskite solar cells. *Adv. Energy Mater.* **5**, 1500279 (2015).
- Nie, W. et al. Light-activated photocurrent degradation and self-healing in perovskite solar cells. *Nat. Commun.* **7**, 11574 (2016).
- Zhang, T. et al. Pinning down the anomalous light soaking effect toward high-performance and fast-response perovskite solar cells: the ion-migration-induced charge accumulation. *J. Phys. Chem. Lett.* **8**, 5069–5076 (2017).
- Tress, W. et al. Interpretation and evolution of open-circuit voltage, recombination, ideality factor and subgap defect states during reversible light-soaking and irreversible degradation of perovskite solar cells. *Energy Environ. Sci.* **11**, 151–165 (2018).
- Unger, E. L. et al. Hysteresis and transient behavior in current-voltage measurements of hybrid-perovskite absorber solar cells. *Energy Environ. Sci.* **7**, 3690–3698 (2014).

10. Sasala, R. A. & Sites, J. R. Time dependent voltage in CuInSe<sub>2</sub> and CdTe solar cells. In Conference Record of the Twenty Third IEEE Photovoltaic Specialists Conference–1993 (Cat. No.93CH3283-9) 543–548 (1993).
11. Listorti, A. et al. The mechanism behind the beneficial effect of light soaking on injection efficiency and photocurrent in dye sensitized solar cells. *Energy Environ. Sci.* **4**, 3494–3501 (2011).
12. Cha, H. et al. An efficient, “Burn in” free organic solar cell employing a nonfullerene electron acceptor. *Adv. Mater.* **29**, 1701156 (2017).
13. Staebler, D. L. & Wronski, C. R. Reversible conductivity changes in discharge-produced amorphous Si. *Appl. Phys. Lett.* **31**, 292–294 (1977).
14. Staebler, D. L., Crandall, R. S. & Williams, R. Stability of n-i-p amorphous silicon solar cells. *Appl. Phys. Lett.* **39**, 733–735 (1981).
15. Street, R. A. Transient photoconductivity studies of the light soaked state of hydrogenated amorphous silicon. *Appl. Phys. Lett.* **42**, 507–509 (1983).
16. Herberholz, R. et al. Phase segregation, Cu migration and junction formation in Cu(In, Ga)Se<sub>2</sub>. *Eur. Phys. J.–Appl. Phys.* **6**, 131–139 (1999).
17. Guillemoles, J.-F. et al. Stability issues of Cu(In,Ga)Se<sub>2</sub>-based solar cells. *J. Phys. Chem. B* **104**, 4849–4862 (2000).
18. Haug, F.-J., Rudmann, D., Zogg, H. & Tiwari, A. N. Light soaking effects in Cu(In,Ga)Se<sub>2</sub> superstrate solar cells. *Thin Solid Films* **431–432**, 431–435 (2003).
19. Stutzmann, M., Jackson, W. B. & Tsai, C. C. Light-induced metastable defects in hydrogenated amorphous silicon: a systematic study. *Phys. Rev. B* **32**, 23–47 (1985).
20. Rau, U., Schmitt, M., Parisi, J., Riedl, W. & Karg, F. Persistent photoconductivity in Cu(In,Ga)Se<sub>2</sub> heterojunctions and thin films prepared by sequential deposition. *Appl. Phys. Lett.* **73**, 223–225 (1998).
21. Hu, J. et al. Photovoltage behavior in perovskite solar cells under light-soaking showing photoinduced interfacial changes. *ACS Energy Lett.* **2**, 950–956 (2017).
22. Liu, G. et al. Irreversible light-soaking effect of perovskite solar cells caused by light-induced oxygen vacancies in titanium oxide. *Appl. Phys. Lett.* **111**, 153501 (2017).
23. deQuilletes, D. W. et al. Photo-induced halide redistribution in organic–inorganic perovskite films. *Nat. Commun.* **7**, 11683 (2016).
24. Godding, J. S. W. et al. Oxidative passivation of metal halide perovskites. *Joule* **3**, 2716–2731 (2019).
25. Slotcavage, D. J., Karunadasa, H. I. & McGehee, M. D. Light-induced phase segregation in halide-perovskite absorbers. *ACS Energy Lett.* **1**, 1199–1205 (2016).
26. Barker, A. J. et al. Detect-assisted photoinduced halide segregation in mixed-halide perovskite thin films. *ACS Energy Lett.* **2**, 1416–1424 (2017).
27. Stranks, S. D. et al. Recombination kinetics in organic-inorganic perovskites: excitons, free charge, and subgap states. *Phys. Rev. Appl.* **2**, 034007 (2014).
28. Guo, D., Andaji-Garmaroudi, Z., Abdi-Jalebi, M., Stranks, S. D. & Savenije, T. J. Reversible removal of intermixed shallow states by light soaking in multication mixed halide perovskite films. *ACS Energy Lett.* **4**, 2360–2367 (2019).
29. Elmelund, T., Seger, B., Kuno, M. & Kamat, P. V. How interplay between photo and thermal activation dictates halide ion segregation in mixed halide perovskites. *ACS Energy Lett.* **5**, 56–63 (2020).
30. Labram, J. G., Perry, E. E., Venkatesan, N. R. & Chabiny, M. L. Steady-state microwave conductivity reveals mobility-lifetime product in methylammonium lead iodide. *Appl. Phys. Lett.* **113**, 153902 (2018).
31. Guo, D., Caselli, V. M., Hutter, E. M. & Savenije, T. J. Comparing the calculated fermi level splitting with the open-circuit voltage in various perovskite cells. *ACS Energy Lett.* **4**, 855–860 (2019).
32. Blackburn, J. L. et al. Measuring photoexcited free charge carriers in mono- to few-layer transition metal dichalcogenides with steady-state microwave conductivity. *J. Phys. Chem. Lett.* **11**, 99–107 (2020).
33. Frost, J. M. & Walsh, A. What is moving in hybrid halide perovskite solar cells? *Acc. Chem. Res.* **49**, 528–535 (2016).
34. Walsh, A. & Stranks, S. D. Taking control of ion transport in halide perovskite solar cells. *ACS Energy Lett.* **3**, 1983–1990 (2018).
35. Crovetto, A. et al. Shining light on sulfide perovskites: LaYS<sub>3</sub> material properties and solar cells. *Chem. Mater.* **31**, 3359–3369 (2019).
36. Savenije, T. J., Ferguson, A. J., Kopidakis, N. & Rumbles, G. Revealing the dynamics of charge carriers in polymer:fullerene blends using photoinduced time-resolved microwave conductivity. *J. Phys. Chem. C* **117**, 24085–24103 (2013).
37. Hong, M. J., Svadlenak, S. R., Goulas, K. A. & Labram, J. G. Thermal stability of mobility in methylammonium lead iodide. *J. Phys. Mater.* **3**, 014003 (2019).
38. Saliba, M. et al. Cesium-containing triple cation perovskite solar cells: improved stability, reproducibility and high efficiency. *Energy Environ. Sci.* **9**, 1989–1997 (2016).
39. Stollerfoht, M. et al. Visualization and suppression of interfacial recombination for high-efficiency large-area pin perovskite solar cells. *Nat. Energy* **3**, 847 (2018).
40. McMeekin, D. P. et al. A mixed-cation lead mixed-halide perovskite absorber for tandem solar cells. *Science* **351**, 151 (2016).
41. Turren-Cruz, S.-H., Hagfeldt, A. & Saliba, M. Methylammonium-free, high-performance, and stable perovskite solar cells on a planar architecture. *Science* **362**, 449–453 (2018).
42. Newport Corporation. Performance Validation Certificate, Oriel SOL1A Class a Solar Simulator. (2018).
43. Herz, L. M. Charge-carrier mobilities in metal halide perovskites: fundamental mechanisms and limits. *ACS Energy Lett.* **2**, 1539–1548 (2017).
44. Miyata, A. et al. Direct measurement of the exciton binding energy and effective masses for charge carriers in organic-inorganic tri-halide perovskites. *Nat. Phys.* **11**, 582–587 (2015).
45. Saeki, A., Yasutani, Y., Oga, H. & Seki, S. Frequency-modulated gigahertz complex conductivity of TiO<sub>2</sub> nanoparticles: interplay of free and shallowly trapped electrons. *J. Phys. Chem. C* **118**, 22561–22572 (2014).
46. Labram, J. G. & Chabiny, M. L. Recombination at high carrier density in methylammonium lead iodide studied using time-resolved microwave conductivity. *J. Appl. Phys.* **122**, 065501 (2017).
47. Reid, O. G. et al. Quantitative analysis of time-resolved microwave conductivity data. *J. Phys. Appl. Phys.* **50**, 493002 (2017).
48. Quitsch, W.-A. et al. The role of excitation energy in photobrightening and photodegradation of halide perovskite thin films. *J. Phys. Chem. Lett.* **9**, 2062–2069 (2018).
49. Perry, E. E., Labram, J. G., Venkatesan, N. R., Nakayama, H. & Chabiny, M. L. N-type surface doping of MAPbI<sub>3</sub> via charge transfer from small molecules. *Adv. Electron. Mater.* **4**, 1800087 (2018).
50. Chin, X. Y., Cortecchia, D., Yin, J., Bruno, A. & Soci, C. Lead iodide perovskite light-emitting field-effect transistor. *Nat. Commun.* **6**, 7383 (2015).
51. Labram, J. G. et al. Temperature-dependent polarization in field-effect transport and photovoltaic measurements of methylammonium lead iodide. *J. Phys. Chem. Lett.* **6**, 3565–3571 (2015).
52. Nomura, K., Kamiya, T. & Hosono, H. Interface and bulk effects for bias–light-illumination instability in amorphous-In–Ga–Zn–O thin-film transistors. *J. Soc. Inf. Disp.* **18**, 789–795 (2010).
53. Lany, S. & Zunger, A. Anion vacancies as a source of persistent photoconductivity in II–VI and chalcopyrite semiconductors. *Phys. Rev. B* **72**, 035215 (2005).
54. Lany, S. & Zunger, A. Light- and bias-induced metastabilities in Cu(In,Ga)Se<sub>2</sub> based solar cells caused by the (VSe–VCu) vacancy complex. *J. Appl. Phys.* **100**, 113725 (2006).
55. Knight, A. J., Patel, J. B., Snaith, H. J., Johnston, M. B. & Herz, L. M. Trap states, electric fields, and phase segregation in mixed-halide perovskite photovoltaic devices. *Adv. Energy Mater.* **10**, 1903488 (2020).
56. McGettrick, J. D. et al. Sources of Pb(0) artefacts during XPS analysis of lead halide perovskites. *Mater. Lett.* **251**, 98–101 (2019).
57. Li, Y. et al. Light-induced degradation of CH<sub>3</sub>NH<sub>3</sub>PbI<sub>3</sub> hybrid perovskite thin film. *J. Phys. Chem. C* **121**, 3904–3910 (2017).
58. Verwey, J. F. Time and intensity dependence of the photolysis of lead halides. *J. Phys. Chem. Solids* **31**, 163–168 (1970).
59. van Berkel, C. & Powell, M. J. Resolution of amorphous silicon thin-film transistor instability mechanisms using ambipolar transistors. *Appl. Phys. Lett.* **51**, 1094–1096 (1987).
60. Kakaliotis, J., Street, R. A. & Jackson, W. B. Stretched-exponential relaxation arising from dispersive diffusion of hydrogen in amorphous silicon. *Phys. Rev. Lett.* **59**, 1037–1040 (1987).
61. Crandall, R. S. Defect relaxation in amorphous silicon: Stretched exponentials, the Meyer-Neldel rule, and the Staebler-Wronski effect. *Phys. Rev. B* **43**, 4057–4070 (1991).
62. Lopes, M. E. et al. Gate-bias stress in amorphous oxide semiconductors thin-film transistors. *Appl. Phys. Lett.* **95**, 063502 (2009).
63. Powell, M. J., van Berkel, C. & Hughes, J. R. Time and temperature dependence of instability mechanisms in amorphous silicon thin-film transistors. *Appl. Phys. Lett.* **54**, 1323–1325 (1989).
64. Wehrspohn, R. B., Powell, M. J. & Deane, S. C. Kinetics of defect creation in amorphous silicon thin film transistors. *J. Appl. Phys.* **93**, 5780–5788 (2003).
65. Mathijssen, S. G. J. et al. Dynamics of threshold voltage shifts in organic and amorphous silicon field-effect transistors. *Adv. Mater.* **19**, 2785–2789 (2007).
66. Libsch, F. R. & Kanicki, J. Bias-stress-induced stretched-exponential time dependence of charge injection and trapping in amorphous thin-film transistors. *Appl. Phys. Lett.* **62**, 1286–1288 (1993).
67. Motti, S. G. et al. Controlling competing photochemical reactions stabilizes perovskite solar cells. *Nat. Photonics* **13**, 532–539 (2019).
68. Jeon, N. J. et al. Solvent engineering for high-performance inorganic–organic hybrid perovskite solar cells. *Nat. Mater.* **13**, 897–903 (2014).
69. Moulder, J. F. *Handbook of X-ray Photoelectron Spectroscopy: A Reference Book of Standard Spectra for Identification and Interpretation of XPS Data*. (Physical Electronics Division, Perkin-Elmer Corporation, Eden Prairie, MN, 1992).

70. Wagner, C. D. et al. Empirical atomic sensitivity factors for quantitative analysis by electron spectroscopy for chemical analysis. *Surf. Interface Anal.* **3**, 211–225 (1981).

### Acknowledgements

We thank Bernard Wenger for insightful discussions. C.L.W. and J.G.L. acknowledge support from the National Science Foundation (grant number: 1902032). Y.-H.L. and H.J.S. acknowledge support from the UK Engineering and Physical Sciences Research Council (grant number: EP/M015254/2). This work was performed, in part, at the Northwest Nanotechnology Infrastructure, a member of the National Nanotechnology Coordinated Infrastructure, which is supported by the National Science Foundation under Grant No. NNCI-1542101. Acquisition of the ambient pressure X-ray photoelectron spectroscopy/ambient pressure scanning tunnelling microscopy system was supported by the National Science Foundation-Major Research Instrumentation program (Grant No. DMR-1429765), the M.J. Murdock Charitable Trust, Oregon BEST, Oregon Nanoscience and Microtechnologies Institute, and Oregon State University.

### Author contributions

J.G.L. conceived the project. C.L.W. carried out SSMC measurements and analysed the data. L.A. carried out TRMC measurements and analysed the data. Y.-H.L. and W.L. prepared the samples. M.J.H. carried out XRD measurements and analysis. R.A. and R.E. performed and analysed XPS measurements. G.S.H., H.J.S., and J.G.L. acquired funding, directed team members, devised strategy, and assisted with interpretation of results. All other authors discussed the results and contributed to the writing of the paper.

### Competing interests

The authors declare no competing interests.

### Additional information

**Supplementary information** is available for this paper at <https://doi.org/10.1038/s42005-020-0350-2>.

**Correspondence** and requests for materials should be addressed to J.G.L.

**Reprints and permission information** is available at <http://www.nature.com/reprints>

**Publisher's note** Springer Nature remains neutral with regard to jurisdictional claims in published maps and institutional affiliations.



**Open Access** This article is licensed under a Creative Commons Attribution 4.0 International License, which permits use, sharing, adaptation, distribution and reproduction in any medium or format, as long as you give appropriate credit to the original author(s) and the source, provide a link to the Creative Commons license, and indicate if changes were made. The images or other third party material in this article are included in the article's Creative Commons license, unless indicated otherwise in a credit line to the material. If material is not included in the article's Creative Commons license and your intended use is not permitted by statutory regulation or exceeds the permitted use, you will need to obtain permission directly from the copyright holder. To view a copy of this license, visit <http://creativecommons.org/licenses/by/4.0/>.

© The Author(s) 2020